Modeling and Measurements of Soot and Species in a Laminar Diffusion Flame

IAN M. KENNEDY* and CLEMENT YAM
Department of Mechanical and Aeronautical Engineering, University of California, Davis, CA 95616

DARRELL C. RAPP and ROBERT J. SANTORO
Department of Mechanical Engineering, The Pennsylvania State University, University Park, PA 16802

A model of laminar, soot-laden ethene diffusion flames has been developed and compared with measurements in nonsooting and sooting flames. Concentrations of stable gas-phase species were measured with mass spectrometry; laser-induced fluorescence was used to measure the OH concentrations. A system of elementary reactions was used to describe the gas-phase chemistry. The model incorporated a simple description of the growth of soot which assumed that acetylene was the only growth species. Soot formation was coupled with the flame chemistry via the loss of acetylene and OH on soot and the production of CO during soot oxidation. The model predicted most of the gas-phase species quite well, with the exception of OH. The loadings of soot in the flames were reproduced adequately, although less success was achieved in predicting the transition from nonsooting to sooting conditions. Details concerning the products of soot oxidation by OH were found to be important with regard to the flame chemistry. The inclusion of soot in the flame model had a significant impact on the predicted structure of the flame as seen in changes to the formation and destruction rates of OH on the fuel side of the flame. The rate of OH reaction with soot in the midregion of the flame was small compared with the rate of reaction of OH with CO. However, the two rates became comparable in the soot burnout zone.

NOMENCLATURE

A	A pre-exponential factor in rate coefficient
C_P	specific heat at constant pressure
D	nozzle diameter
D_n	effective diffusivity of species n in the mixture
E	activation energy
f	mixture fraction
g	gravitational acceleration
h_n	specific enthalpy of species n
k	rate coefficient
M_n	molecular weight of species n
N	number of species
q^R	divergence of the radiative heat flux vector
R	gas constant
r	radial distance
S	source or sink term for soot equation
T	temperature
u	velocity in the axial direction
v	velocity in the radial direction
v_{n_T}	normal diffusion velocity of species n
v_n^{corr}	thermal diffusion velocity of species n
V_n^{corr}	correction to diffusion velocities
V_T	thermophoretic velocity of soot particles
$\dot{w}_n$	reaction rate of species n
X_n	mole fraction of species n
x	distance along the axis
Y_n	mass fraction of species n

Greek Symbols

β	exponent on temperature in rate coefficient
κ_n	thermal diffusion ratio
λ	thermal conductivity
μ	absolute viscosity
ν	kinematic viscosity
ρ	density

Subscripts

eq	equilibrium
g	soot mass growth
n	soot nucleation
o	soot oxidation

* Corresponding author.

0010-2180/96/$15.00
PII S0010-2180(96)00092-2

COMBUSTION AND FLAME 107: 368–382 (1996)

Published by Elsevier Science Inc.

INTRODUCTION

Detailed descriptions of chemical kinetics in premixed flames and laminar counterflow diffusion flames have been extended by various researchers to include reactions leading to the formation of polyaromatic hydrocarbons (PAH) and soot [1–5]. Less attention has been given to the more complex phenomena in an axisymmetric co-flowing diffusion flame, in which the fate of PAH and soot depends on the details of the flow field with spatially distinct regions of formation and oxidation. Studies of this configuration have neglected either the interaction of flame chemistry and soot formation in which soot growth acts as a sink of growth species such as acetylene [6] or have neglected the impact of OH reactions with soot that can act as a source of species such as CO [7].

Previous studies of an axisymmetric laminar ethene–air diffusion flame have suggested that the modeling of soot formation with the assumption of equilibrium chemistry may underestimate significantly the superequilibrium concentrations of important radicals such as O and OH [8, 9]. These species are important oxidants of soot, particularly near the tip of diffusion flames where soot can escape. The assumption of equilibrium for all the gas-phase reactions [8–10] cannot yield accurate estimates of these species; finite rate chemistry is required in order to relax this assumption. Hence, a reduced set of elementary chemical reactions has been incorporated into a parabolic code that solves the boundary layer form of the conservation equations for mass, momentum, and energy conservation. A more accurate representation of radical concentrations has been achieved. The purpose of the investigation was to explore the potential interaction of soot formation with flame chemistry, in particular the fate of OH. Consequently, a slightly modified version of the simple, semi-empirical soot model of Fairweather et al. [11] was used to provide realistic estimates of soot growth rates and soot volume fractions. It was not the intention of this study to elaborate on the soot modeling by incorporating detailed reactions [5, 12] for PAH and soot or to incorporate details with regard to soot morphology [13]. The results of the modeling have been compared with the results of an experimental program at The Pennsylvania State University.

EXPERIMENTAL METHOD

An atmospheric pressure, laminar ethene–air diffusion flame was established on a coannular burner under conditions identical to the nonsooting flame that was investigated by Santoro et al. [14]; only a brief description will be given here. This burner consisted of an 11.1-mm diameter brass fuel tube surrounded by a 102-mm diameter air annulus. A brass cylindrical chimney was used to shield the flame from laboratory air currents with access for sampling provided by slots machined in the chimney wall. The ethene (C_2H_4) and air flow rates were 3.85 $cm^3\ s^{-1}$ and 713 $cm^3\ s^{-1}$, respectively, which were measured with calibrated rotameters. Ethene with a stated purity of 99.5% was used; dried, filtered air was supplied by an in-house compressor.

Radial profile measurements of species concentrations have been obtained throughout the flame using a quartz microprobe. Quartz microprobes have been used in many studies to extract gas samples from premixed flames [15, 16] and diffusion flames [17–21]. Until recently, their use has been limited to regions where the soot volume fraction is low to avoid clogging the probe orifice. A variation of the standard quartz microprobe design, referred to as an electro-mechanical sonic (EMS) probe, was developed by Puri [21] and enabled sampling in flame regions where soot volume fractions were on the order of 10^{-5}. This probe has a fiber which extends through the orifice and is attached to a solenoid core with springs on either side of the core. A solenoid is placed around the outside of the quartz tube and the current to the solenoid is interrupted at about 30 Hz, providing for constant motion of the fiber in the orifice, thus keeping an annular region open for gas sampling. The fiber is $\approx 125\ \mu m$ in diameter and is made from sapphire, while the orifice diameter is $\approx 190\ \mu m$. The annular sampling region has an area equivalent to an orifice of approximately 130 μm diameter.

A mass spectrometer (MS) was used to analyze the samples; the MS analysis was verified

by gas chromatography (GC). The use of these two techniques offered an independent verification of the concentration profile measurements as well as providing specific-species measurement capability as described below. In general, the two analytical approaches yielded agreement to within ±20%. Because of difficulties in detecting H_2 with the GC, the composition measurements reported in this paper were derived from the MS analysis.

The mass spectrometer employed an Extrel model 7-324-9 quadrupole mass filter with a mass range of 1–500 amu for separation of ions and an electron multiplier for detection. Calibration of the MS followed the method used by Ermolin et al. [22], which is mathematically similar to that of Bittner [23] and Crowhurst and Simmons [19]. The method assumes that the signal response of a particular species relative to other species remains constant. That is, given the same mixture, the signals of any two gases will always be in the same ratio and, therefore, independent of the mass flow rate through the orifice. Hence, the measurements are not susceptible to any possible orifice clogging or variations in density. Secondly, this method assumes that the species measured constitute all of the gases present and they are normalized to a mole fraction of one.

A limitation of the MS in this flame is the coincidence of C_2H_4, N_2, and CO at mass 28. For C_2H_4, the fragment at mass 27 is used as an independent measurement. Calibration of C_2H_4 at both masses 27 and 28 is necessary so that the signal contribution of C_2H_4 at mass 28 can be subtracted from the mass 28 signal. Hydroxyl radical ($OH\cdot$) concentration measurements were obtained in a previous study; details were reported by Puri et al. [8].

NUMERICAL MODEL

The most general formulation of the governing equations consists of the compressible Navier–Stokes equations, an equation to describe the conservation of energy, and species transport equations; the equations are elliptic. The computer time to solve these fully elliptic equations is large [24] in comparison to a parabolic code that solves the equations with a boundary layer assumption. In order to keep the computational cost within reasonable limits, a code was written to solve the boundary layer forms of the governing equations in cylindrical coordinates with zero pressure gradient. Hence, the equations could be solved with a marching method. It is expected that the boundary layer assumption will introduce the greatest errors in the vicinity of the nozzle exit. The flame that has been investigated in this study is relatively long, of the order of seven nozzle diameters. Therefore, it is anticipated that the errors will not be large in the region of most interest to soot oxidation and radiation, and their impact on gas-phase chemistry.

The equations are solved in primitive variable form. Hence, the steady-state continuity equation

$$\frac{\partial(\rho u)}{\partial x} + \frac{1}{r}\frac{\partial}{\partial r}(r\rho v) = 0 \tag{1}$$

is solved along with the equation for axial momentum

$$\rho u\frac{\partial u}{\partial x} + \rho v\frac{\partial u}{\partial r} = \frac{1}{r}\frac{\partial}{\partial r}\left(\mu r\frac{\partial u}{\partial r}\right) + \rho g. \tag{2}$$

The energy equation is written in terms of the temperature as

$$\begin{aligned}\rho C_P\left(u\frac{\partial T}{\partial x} + v\frac{\partial T}{\partial r}\right) &= \frac{1}{r}\frac{\partial}{\partial r}\left(r\lambda\frac{\partial T}{\partial r}\right) + q^R \\ &\quad - \frac{1}{r}\frac{\partial}{\partial r}\left(r\rho T\sum_{n=1}^{N} Y_n C_{P,n} V_n\right) \\ &\quad - \sum_{n=1}^{N} M_n h_n \dot{w}_n,\end{aligned} \tag{3}$$

in which the complete diffusion velocity of species n is V_n:

$$V_n = v_n + v_n^T + V_n^{\text{corr}}. \tag{4}$$

The divergence of the radiative heat flux is represented by q^R. The code includes a radiation model in which an optically thin approximation for the emission by soot is adopted for simplicity [9, 10]. Gas radiation has been ig-

nored in view of the relatively strong luminosity of soot in ethene diffusion flames. The application of this simple radiation model is justified a posteriori by comparison with temperature measurements. The normal diffusion velocity of species n is given by

$$v_n = -\frac{D_n}{Y_n}\frac{\partial Y_n}{\partial r}, \tag{5}$$

and the contribution of the thermal diffusion phenomenon to the total diffusion velocity is given by

$$v_n^T = \frac{D_n \kappa_n}{X_n}\frac{1}{T}\frac{\partial T}{\partial r}. \tag{6}$$

The thermal diffusion ratio, κ_n, was obtained from the Sandia transport properties package [25]. A correction diffusion velocity V_n^{corr},

$$V_n^{\text{corr}} = -\sum_1^N Y_n\left(v_n + v_n{}^T\right), \tag{7}$$

ensures that the net diffusive flux of all gaseous species is zero. An equation is solved for $N-2$ species mass fractions in the gas phase

$$\rho u\frac{\partial Y_n}{\partial x} + \rho v\frac{\partial Y_n}{\partial r} = -\frac{1}{r}\frac{\partial}{\partial r}\{r\rho Y_n V_n\} + M_n\dot{w}_n, \tag{8}$$

with the $N-1$th species being soot and the Nth being N_2. The explicit form of the equation for the soot mass fraction, Y_{soot}, is

$$\rho u\frac{\partial Y_{\text{soot}}}{\partial x} + \rho v\frac{\partial Y_{\text{soot}}}{\partial r} = -\frac{1}{r}\frac{\partial}{\partial r}\{r\rho V_T Y_{\text{soot}}\} + S(Y_{\text{soot}}, T, Y_{C_2H_2}, Y_{O_2}, Y_{OH}, N). \tag{9}$$

In this equation, the thermophoretic velocity is found from the appropriate expression for a free molecular aerosol [26]:

$$V_T = -0.55\frac{v}{T}\frac{\partial T}{\partial r}. \tag{10}$$

The source term in Eq. 9 includes the contributions of soot nucleation ($\dot{w}_{\text{nucl}}$), soot surface growth ($\dot{w}_g$) and soot oxidation ($\dot{w}_o$).

$$S = \dot{w}_{\text{nucl}} + \dot{w}_g - \dot{w}_o. \tag{11}$$

The latter term has two contributions, viz., oxidation of soot by O_2 and by OH to form CO.

Earlier modeling studies of soot formation used an average number density to obtain an estimate of the soot aerosol surface area [10]. The present study follows the approach of Fairweather et al. [27] in solving an equation for the number density of particles. The soot model implicitly assumes that the coagulation of soot gives rise to a spherical particle. It should be noted that their equation for the particle number density did not incorporate the effect of thermophoresis. Various authors [28, 29] have pointed out the necessity of writing the balance equation in terms of a particle velocity that may include a thermophoretic contribution and a Brownian contribution. We ignore the very small influence of Brownian diffusion of soot particles. Hence, the fundamental equation for the steady-state balance of particle number density, N, is written in terms of the particle velocity, $\vec{u}_P$ as

$$\nabla\cdot\left(\vec{u}_P N\right) = S_N, \tag{12}$$

where S is a source term (coagulation or nucleation). The velocity of a soot particle is the sum of the gas velocity and the thermophoretic velocity if Brownian diffusion is ignored. In that case, with the aid of the continuity equation, Eq. 12 can be rewritten in terms of the particle number density per unit mass of gas, defined as

$$n = \frac{N}{\rho}, \tag{13}$$

as follows:

$$\rho u\frac{\partial n}{\partial x} + \rho v\frac{\partial n}{\partial r} = -\frac{1}{r}\frac{\partial}{\partial r}\{r\rho V_T n\} + S_N. \tag{14}$$

The formulation of the nucleation, coagulation, and growth rates is identical to the model of Fairweather et al. [27]. The model assumes

that all the soot mass growth can be attributed to acetylene, C_2H_2. The nucleation and soot growth rates in Eqs. 9 and 12 are first order in C_2H_2. The growth rate of soot is assumed to be also a function of the soot aerosol surface area. The aerosol is assumed to be monodisperse, and the area is found from the number density of particles, N, and the soot mass fraction.

The model of Fairweather et al. [27] has been adopted in its entirety with the following important difference. The rate of soot surface growth has been increased by a factor of 2 to yield an adequate representation of the measured soot volume fractions in the flame. This ad hoc action is justified as follows. Fairweather et al. [27] did not incorporate the impact of OH in their model. The oxidation of soot was attributed entirely to O_2. The parameters in their model were calibrated against experiments on this basis. As a result, their soot growth model underpredicts the measured soot volume fractions when it is used in our calculations which include OH oxidation. Differences in the particle morphology between their conditions and our conditions may also contribute to the observed discrepancy. We find that a factor of 2 yields satisfactory results.

Particular attention has been given to the correct formulation of the oxidation mechanism in the present model. We have implemented the Nagle Strickland-Constable [30] formula for O_2 oxidation of soot. The product of the reaction was assumed to be CO. Oxidation of soot by OH was generally more important in most of the flame and, hence, it required greater attention than the O_2 mechanism. Calculations were originally performed with the approach that was adopted by Kennedy et al. [10], i.e., a collision efficiency of 0.1 was used for the reaction of OH with soot. This approximate value of the collision efficiency was derived from the measurements of Neoh et al. [31], later confirmed by Roth et al. [32]. However, we found that a constant value for the collision efficiency, regardless of its magnitude, could not faithfully reproduce the characteristics of the soot distribution in a flame. Consequently, we made use of the results of Puri et al. [33], who found that the apparent collision efficiency of OH with soot changed with time and/or temperature. A revised estimate of the oxidation rate of soot by O_2 [34] led to some uncertainty in the conclusions of the authors. However, despite the revised estimates of O_2 oxidation rates, their results in a methane–butane flame continued to show a trend to higher collision efficiencies between soot and OH with increasing residence times. Because it was not possible to calculate soot reactivities in the manner of Frenklach and Wang [5] with this simple soot model, the variation of soot reactivity with time has been accounted for in the manner illustrated in Fig. 1. The collision efficiency was assumed to vary linearly with distance from the fuel nozzle, from a minimum of 0.05 to a maximum of 0.2 at the flame tip. This model of reactivity achieved reasonable results, although it is quite crude. We found that it was important to incorporate this variation in collision efficiency to obtain satisfactory results. The use of a constant value of the collision efficiency at the upper end of the range resulted in too little soot throughout the flame; use of a constant value at the low end of the range did not give rise to sufficient burnout of soot at the end of the flame. Assumptions with regard to the product of the attack of OH on soot were found to be important, as discussed below. In the present model, the following irreversible, global reaction was used:

$$C_i + OH \rightarrow C_{i-1} + CO + \tfrac{1}{2}H_2, \qquad 1.$$

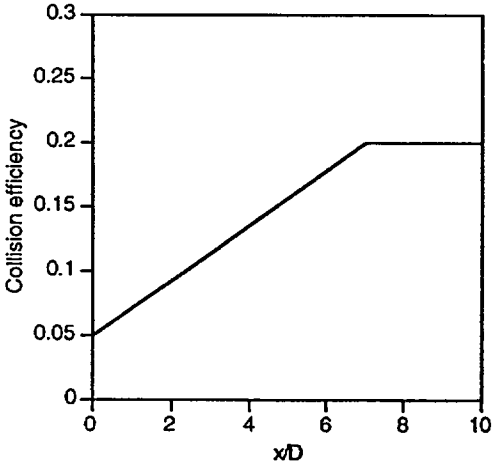

Fig. 1. OH collision efficiency with soot as a function of nondimensional distance from nozzle.

in which C_i is a soot particle with i carbon atoms. Other reaction products may be possible. For example, Mauss et al. [1] used the following reaction to describe OH attack on soot:

$$C_{i+1}H + OH \rightarrow C^*_{i-1} + CH + CHO, \qquad 2.$$

where $C_{i+1}H$ was a so-called armchair site on a soot particle and C^*_{i-1} was the corresponding radical. Unfortunately, no direct experimental evidence exists with regard to the products of OH reactions with soot. It is not certain that one mechanism should be favored over another. Reaction 1 was used in these calculations.

Method of Solution

Initial Conditions

Initial conditions for all the major species as well as the temperature profiles were required in order to start the calculation. These conditions were generated by solving simultaneously the momentum, continuity, and mixture fraction [35] equations on the computational grid from the nozzle exit up to a short distance from the nozzle. Once the mixture fraction profile was known, all the other dependent scalar variables could be obtained through equilibrium thermochemistry [36]. Detailed chemistry was used beyond this point. Numerical trials established that reasonable initial conditions for the finite rate chemistry calculation could be obtained by using the mixture fraction/equilibrium calculation up to 0.1 nozzle diameters. The predictions at the downstream points of interest were not sensitive to variations in the location of the switch from equilibrium to finite rate chemistry. The flow from the nozzle was taken to be pure fuel. The co-flow air extended to infinity, i.e., there was no confining cylinder.

Chemical Mechanism

A simplified mechanism was used to describe concisely the C_1 and the C_2 reactions for ethene oxidation. The methane mechanism of Smooke et al. [37] was found to be numerically efficient, and it has been implemented in the current code with the rates for all the C_1 chemistry from Smooke et al. [37]. Although it was intended primarily for lean combustion, it contained a sufficient degree of detail to describe methane oxidation for our purposes in the laminar diffusion flame. The "skeletal" mechanism omitted several reactions, such as the CH_3 recombination reaction that can lead to ethane formation. Our primary interest in the ethene flame was in the concentrations of acetylene; the recombination of methyl radicals is not likely to have a major impact on the predictions of acetylene in the ethene flame. This is borne out by later comparisons with experimental data.

The C_2 chemistry was described by a series of reactions that convert C_2H_4 to C_2H_3 and C_2H_2. The immediate source of the rates for the C_2 reactions was Frenklach et al. [4]; primary sources of the rate data may be found in that reference. Most of the reactions for ethene and acetylene formation and consumption that Leung and Lindstedt [38] found to be important in alkane diffusion flames were included in the current mechanism. For example, the important reactions of ethene with H atoms (Reaction 63) and the decomposition of vinyl to acetylene (Reaction 60) were included. Furthermore, the reactions of O atoms and OH with acetylene (Reactions 54 and 55) were included.

The entire reaction mechanism is shown in Table 1 and is composed of 64 reactions involving 24 species. The rates of reverse reactions were derived from the corresponding equilibrium constants. The thermochemical data in CHEMKIN [39] were used to obtain the equilibrium constants.

Numerical Scheme

The governing differential equations were written in a discrete form by using a second order accurate scheme for the diffusion terms and first order accurate scheme for the convective terms with the delta formulation. The nonlinear terms (convective and rate terms) were linearized by Newton's method. The resulting Jacobian matrices were determined numerically in the manner described by Smooke and Giovangigli [40]. The Jacobian did not need to be updated continuously since the changes from one step to the next were small. We

TABLE 1

Chemical Reaction Mechanism in the Form $k = AT^{\beta}e^{-E/RT}$ (units are moles, cubic centimeters, seconds, Kelvin, and calories per mole)

Reaction*	A	β	E
3. $H_2 + O_2 \Leftrightarrow 2OH$	1.70E + 13	0	47780.
4. $OH + H_2 \Leftrightarrow H_2O + H$	1.17E + 09	1.3	3626.
5. $H + O_2 \Leftrightarrow OH + O$	2.20E + 14	0	16800.
6. $O + H_2 \Leftrightarrow OH + H$	1.80E + 10	1.0	8826.
7. $H + O_2 + M \Leftrightarrow HO_2 + M$	2.10E + 18	−1.0	0
8. $H + O_2 + O_2 \Leftrightarrow HO_2 + O_2$	6.70E + 19	−1.4	0
9. $H + O_2 + N_2 \Leftrightarrow HO_2 + N_2$	6.70E + 19	−1.4	0
10. $OH + HO_2 \Leftrightarrow H_2O + O_2$	5.00E + 13	0	1000.
11. $H + HO_2 \Leftrightarrow 2OH$	2.50E + 14	0	1900.
12. $O + HO_2 \Leftrightarrow O_2 + OH$	4.80E + 13	0	1000.
13. $2OH \Leftrightarrow O + H_2O$	6.00E + 08	1.3	0
14. $H_2 + M \Leftrightarrow H + H + M$	2.23E + 12	5	92600.
15. $O_2 + M \Leftrightarrow O + O + M$	1.85E + 11	5	95560.
16. $H + OH + M \Leftrightarrow H_2O + M$	7.50E + 23	−2.6	0
17. $H + HO_2 \Leftrightarrow H_2 + O_2$	2.50E + 13	0	700.
18. $HO_2 + HO_2 \Leftrightarrow H_2O_2 + O_2$	2.00E + 12	0	0
19. $H_2O_2 + M \Leftrightarrow OH + OH + M$	1.30E + 17	0	45500.
20. $H_2O_2 + H \Leftrightarrow HO_2 + H_2$	1.60E + 12	0	3800
21. $H_2O_2 + OH \Leftrightarrow H_2O + HO_2$	1.00E + 13	0	1800.
22. $HCO + OH \Leftrightarrow CO + H_2O$	5.00E + 12	0	0
23. $HCO + M \Leftrightarrow H + CO + M$	1.60E + 14	0	14700.
24. $HCO + H \Leftrightarrow CO + H_2$	4.00E + 13	0	0
25. $HCO + O \Leftrightarrow OH + CO$	1.00E + 13	0	0
26. $HCO + O_2 \Leftrightarrow HO_2 + CO$	3.00E + 12	0	0
27. $HO_2 + CO \Leftrightarrow CO_2 + OH$	5.80E + 13	0	22934.
28. $CO + O + M \Leftrightarrow CO_2 + M$	3.20E + 13	0	−4200.
29. $CO + OH \Leftrightarrow CO_2 + H$	1.51E + 07	1.3	−758.
30. $CO + O_2 \Leftrightarrow CO_2 + O$	1.60E + 13	0	41000.
31. $CH_4 + M \Leftrightarrow CH_3 + H + M$	1.00E + 17	0	86000.
32. $CH_4 + O_2 \Leftrightarrow CH_3 + HO_2$	7.90E + 13	0	56000.
33. $CH_4 + H \Leftrightarrow CH_3 + H_2$	2.20E + 04	3.0	8750.
34. $CH_4 + O \Leftrightarrow CH_3 + OH$	1.60E + 06	2.4	7400.
35. $CH_4 + OH \Leftrightarrow CH_3 + H_2O$	1.60E + 06	2.1	2460.
36. $CH_2 + OH \Leftrightarrow CH_2O + H$	3.00E + 13	0	0
37. $CH_2 + O_2 \Leftrightarrow CO + OH + H$	3.10E + 13	0	0
38. $CH_2O + OH \Leftrightarrow HCO + H_2O$	7.53E + 12	0	167.
39. $CH_2O + H \Leftrightarrow HCO + H_2$	3.31E + 14	0	10500.
40. $CH_2O + M \Leftrightarrow HCO + H + M$	3.31E + 16	0	81000.
41. $CH_2O + O \Leftrightarrow HCO + OH$	1.81E + 13	0	3082.
42. $CH_3 + O_2 \Leftrightarrow CH_3O + O$	7.00E + 12	0	25652.
43. $CH_3O + M \Leftrightarrow CH_2O + H + M$	2.40E + 13	0	28812.
44. $CH_3O + H \Leftrightarrow CH_2O + H_2$	2.00E + 13	0	0
45. $CH_3O + OH \Leftrightarrow CH_2O + H_2O$	1.00E + 13	0	0
46. $CH_3O + O \Leftrightarrow CH_2O + OH$	1.00E + 13	0	0
47. $CH_3O + O_2 \Leftrightarrow CH_2O + HO_2$	6.30E + 10	0	2600.
48. $CH_3 + O_2 \Leftrightarrow CH_2O + OH$	5.20E + 13	0	34574.
49. $CH_3 + O \Leftrightarrow CH_2O + H$	6.80E + 13	0	0
50. $CH_3 + OH \Leftrightarrow CH_2O + H_2$	7.50E + 12	0	0
51. $C_2H + H_2 \Leftrightarrow C_2H_2 + H$	1.10E + 13	0	2868.
52. $C_2H + O_2 \Leftrightarrow HCCO + O$	6.02E + 11	0	0
53. $HCCO + H \Leftrightarrow CH_2 + CO$	1.50E + 14	0	0
54. $C_2H_2 + O \Leftrightarrow CH_2 + CO$	7.81E + 03	2.8	502.
55. $C_2H_2 + OH \Leftrightarrow HCCOH + H$	5.06E + 05	2.3	13496.
56. $CH_2CO + H \Leftrightarrow HCCO + H_2$	3.00E + 13	0	8599.
57. $CH_2CO + OH \Leftrightarrow HCCO + H_2O$	1.00E + 13	0	2627.

*Reactions (1) and (2) appear in the text. They are excluded from this table due to their lack of rate constants.

TABLE 1 (Continued)

Chemical Reaction Mechanism in the Form $k = AT^{\beta}e^{-E/RT}$ (units are moles, cubic centimeters, seconds, Kelvin, and calories per mole)

Reaction	A	β	E
58. $C_2H_3 + O \Leftrightarrow CH_2CO + H$	3.00E + 13	0	0
59. $C_2H_3 + O_2 \Leftrightarrow CH_2O + HCO$	4.00E + 12	0	−239.
60. $C_2H_3 + M \Leftrightarrow C_2H_2 + H + M$	2.00E + 38	−7.2	50567.
61. $C_2H_4 + OH \Leftrightarrow C_2H_3 + H_2O$	3.00E + 13	0	2986.
62. $C_2H_4 + M \Leftrightarrow C_2H_2 + H_2 + M$	2.60E + 17	0	79230.
63. $C_2H_4 + H \Leftrightarrow C_2H_3 + H_2$	3.16E + 11	0.7	8002.
64. $C_2H_4 + O \Leftrightarrow CH_3 + HCO$	1.60E + 08	1.4	525.

found that the re-evaluation of the Jacobian at every fifth axial step yielded the same results as an evaluation at every step.

The resulting sets of coupled algebraic equations were solved implicitly and simultaneously by a block solver with iterations to account for the nonlinear term. Typically, eight iterations per step were required to converge the equations to a local solution. The step size (Δx) was determined by limiting the maximum changes of all the dependent variables by no more than 10%. If the changes in any dependent variable exceeded this limit, the solution was rejected, a smaller Δx was used, and the calculation was redone. The equations were assumed to be solved when the residual approached machine zero. If a local convergence could not be reached, a smaller Δx was used and the solution was recalculated.

Grid adaptation was used in order to resolve the high gradient region in the flow field with a minimum number of grid points. This was achieved by adapting the grid distribution to the temperature gradient. The results shown in this report were obtained by using only 61 points in the transverse direction. All the properties of the fluid, the diffusion coefficients of all species, and the chemical source term for each species were obtained by using CHEMKIN [39] and the accompanying transport library [25].

RESULTS

Most of the experimental data were obtained in the nonsooting flame (fuel flow rate of 3.85 $cm^3\ s^{-1}$) and, hence, greater attention has been given to predicting the structure of that flame. A sooting flame has also been calculated with a fuel flow rate of 4.90 $cm^3\ s^{-1}$; predictions of the integrated soot volume fractions in that flame are shown later. Experimental data for temperatures, velocities, and soot volume fractions are derived from the earlier studies of Santoro et al. [41]. The first test of the flow field model is the reproduction of the velocity field. Figure 2 compares the radial distribution of the axial velocity at 20 mm from the burner nozzle with experimental results; results are also shown for a location near the tip of the flame. Satisfactory agreement was obtained with a simplified boundary layer model of the flow. The acceleration of the flow as a result of buoyancy is evident in the increase in the axial velocity by a factor of 2 along the flame.

Coupling between the soot production and the luminous radiative heat loss via the impact

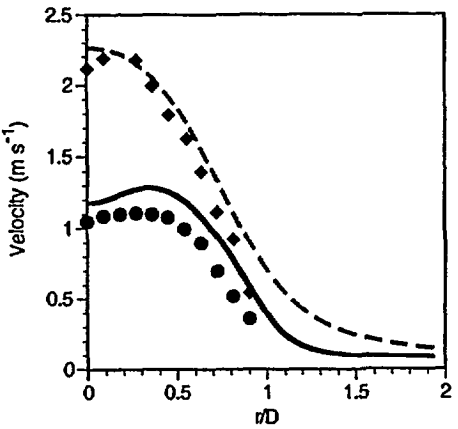

Fig. 2. Measured (Santoro et al. [41]) and predicted axial velocity profiles at: ● experimental points 20 mm from fuel nozzle in the nonsooting flame; —— calculated results 20 mm from fuel nozzle in the nonsooting flame; ♦ 70 mm from fuel nozzle in the nonsooting flame; - - - calculated results 70 mm from fuel nozzle in the nonsooting flame.

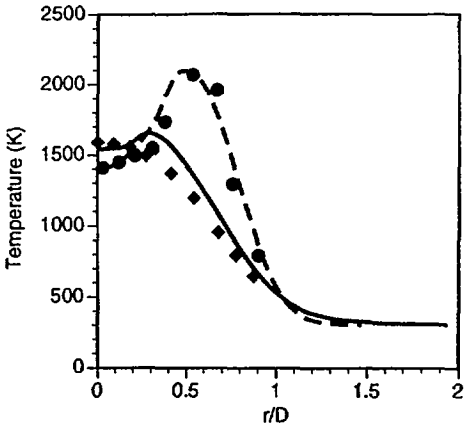

Fig. 3. Measured (Santoro et al. [41]) and predicted temperature profiles at ● experimental points 20 mm from fuel nozzle in the nonsooting flame; - - - calculated results 20 mm from fuel nozzle in the nonsooting flame; ♦ 70 mm from fuel nozzle in the nonsooting flame; —— calculated results 70 mm from fuel nozzle in the nonsooting flame.

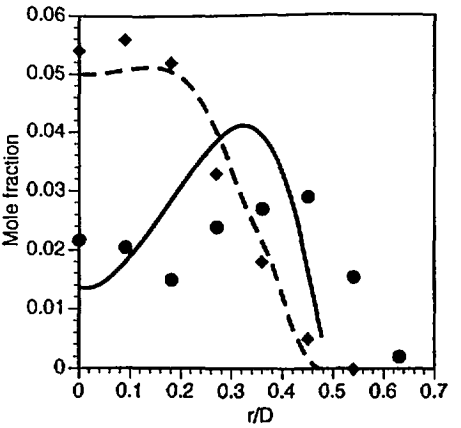

Fig. 4. Measured and predicted C_2H_2 mole fractions at: ● experimental points 7 mm from fuel nozzle in the nonsooting flame; —— calculated results 7 mm from fuel nozzle in the nonsooting flame; ♦ experimental points 20 mm from fuel nozzle in the nonsooting flame; - - - calculated results 20 mm from fuel nozzle in the nonsooting flame.

of the latter phenomenon on temperatures is an essential aspect of hydrocarbon diffusion flames. A comparison of the measured and predicted temperature fields offers a measure of the accuracy of the simple radiation model. Figure 3 presents radial profiles of the measured and predicted temperatures at two axial locations in the nonsooting flame. The drop in the peak temperature at the more downstream location is evidence of the heat loss due to luminous radiation (the contributions of CO_2 and H_2O to radiation losses were not included). The agreement in the temperature field is good.

Profiles of C_2H_2 mole fractions are shown in Fig. 4 for two locations. Satisfactory predictions of acetylene are essential because the growth rate of soot is directly dependent on acetylene concentration in the present soot model. The agreement with the measured acetylene mole fractions is found to be satisfactory. Hydrogen (not shown) is also predicted generally very well by the code.

A measure of the accuracy of the soot model is given by the calculation of the integrated soot volume fraction (Fig. 5). This quantity is obtained by integrating the soot volume fraction across the flame. It indicates the total amount of soot at a given axial location in the flame. The agreement between the measurements of Santoro et al. [41] and the calculations is very good. The model is able to reproduce the peak integrated soot volume fraction as well as predict the burnout of soot at the flame tip. Detailed comparisons of the radial distribution of soot in the flame are offered in Figs. 6 and 7 at 15 mm and 50 mm from the nozzle, respectively. In both cases, the maximum soot volume fraction is captured quite well by the model. However, the presence of significant amounts of soot on the centerline of the flame at a position 50 mm from the nozzle is not predicted. In order to reproduce this

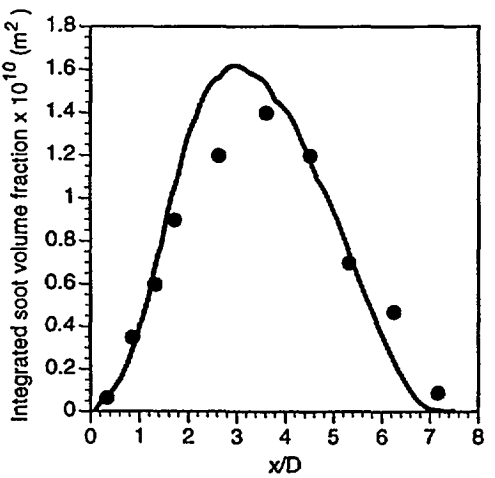

Fig. 5. Integrated soot volume fractions in the nonsooting flame (points are measurements from Santoro et al. [41]).

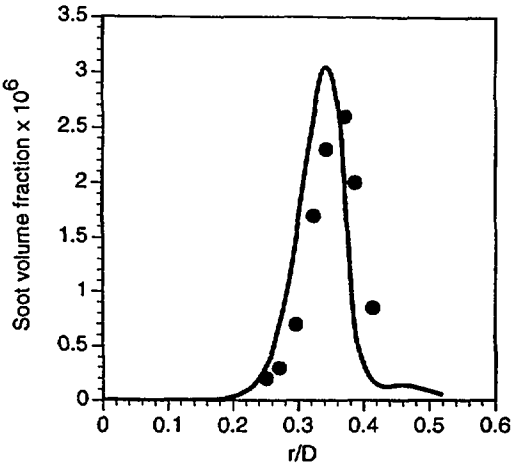

Fig. 6. Measured (Santoro et al. [41]) and predicted (solid line) soot volume fractions at 15 mm from fuel nozzle in the nonsooting flame.

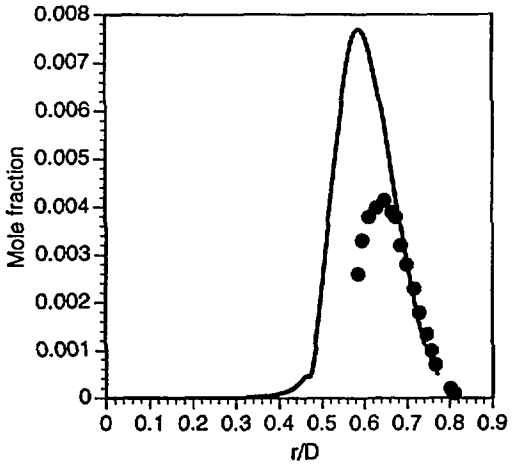

Fig. 8. Measured (Santoro et al. [41]) and predicted (solid line) OH mole fractions at 7 mm from fuel nozzle in the nonsooting flame.

behavior, a more detailed soot model is required, one that accounts for soot formation from PAH [5] that are known to form on the axis of diffusion flames [42].

Hydroxyl mole fractions have been measured with laser-induced fluorescence (LIF). The calculated hydroxyl mole fractions are compared with the measurements at 7 mm and 70 mm in Figs. 8 and 9, respectively. The model tends to overpredict the OH mole fractions throughout the flame. However, it should be borne in mind that LIF measurements involve uncertainties that are related to quenching corrections and other errors. The errors were estimated to be $\pm 50\%$ [21]. The numerical model reproduces the measured trend in OH mole fractions with distance from the nozzle. The concentrations of OH decrease as the flame tip is approached due to the drop in temperature and due to the loss of OH by reaction with soot particles and CO.

The presence of soot in regions containing OH in a diffusion flame can affect the flame structure and chemistry. It is of interest to examine the net rate of production of OH by gas-phase chemistry and to compare that rate

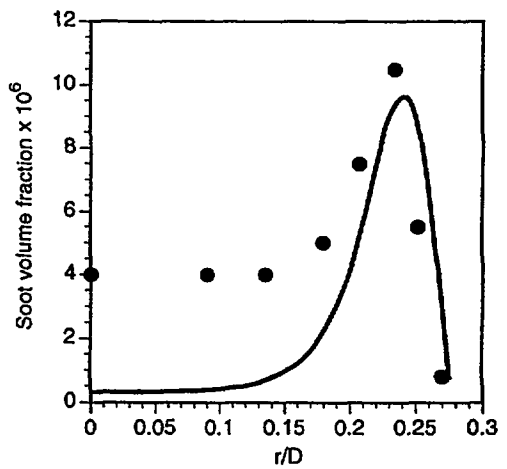

Fig. 7. Measured (Santoro et al. [41]) and predicted (solid line) soot volume fractions at 50 mm from fuel nozzle in the nonsooting flame.

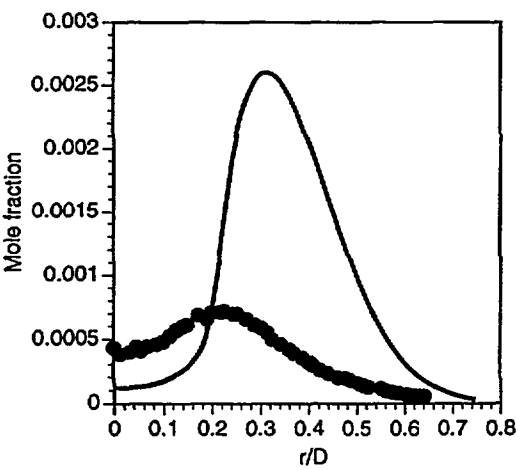

Fig. 9. Measured (Santoro et al. [41]) and predicted (solid line) OH mole fractions at 70 mm from fuel nozzle in the nonsooting flamed.

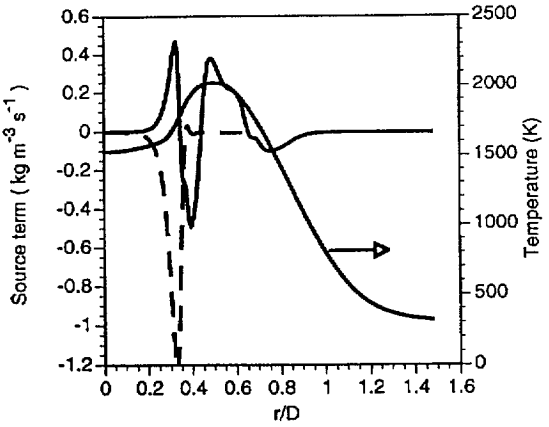

Fig. 10. Net rate of formation or destruction of OH by gas-phase reactions (solid line); rate of loss of OH on soot particles (dashed line); temperature at 40 mm from nozzle in nonsooting flame.

with the loss rate of OH on soot. Figure 10 shows the net rate of OH production or destruction by gas-phase processes and its loss rate on soot particles along with the temperature. The peak formation rate of OH is located near the center of the reaction zone. There is a strong destruction rate of OH on the fuel side of the flame front as a result of OH reactions with hydrocarbon species. A secondary zone of OH formation is apparent in Fig. 10 on the rich side of the flame. This feature is not usually seen in flame structure calculations in the absence of soot and is certainly absent in the present calculations lower in the flame.

The strong rate of OH production on the rich side of the flame is surprising. Analysis of the reaction rates, and recomputation without a soot model, indicate that the change to the OH production or destruction profile in this region is associated with the presence of soot in the flame. The dominant source of OH in this rich region of the flame is the reverse of Reaction 4 viz.,

$$H_2O + H \leftrightarrow OH + H_2.$$

The rate of formation of OH by this reaction was unchanged by the presence or absence of soot in the calculations. The main gas-phase sinks of OH on the fuel side of the flame for the present reaction scheme were Reactions 36 and 13. These sinks of OH balance production by Reaction 4 without soot. The code has been run with and without the soot model in place. It was found that the appearance of a source of OH on the fuel side was due, in fact, to the decrease in the rates of these destruction reactions as a result of a drop in the concentrations of CH_2 and OH, respectively. The decrease in the concentrations of these species is related to the temperature drop when soot radiation is present and also to the scavenging of C_2H_2 and OH by soot. It may be argued that this phenomenon accounts for the overprediction of OH concentrations (Figs. 8 and 9) and is not authentic. Although the calculated OH reaction rates may be to some extent an artifact of the simplified kinetics, the observations point out the potential impact that soot can have on the chemical structure of a diffusion flame. In particular, it highlights the possible difficulty in achieving accurate predictions of OH concentrations, and hence of soot oxidation, with simplified chemical kinetics.

The emission of soot from a flame is often associated with the emission of CO. Puri et al. [33] considered the competition between soot and CO for OH. They found that the rate of CO + OH dominated the rate of C_i(soot) + OH in a methane flame. However, in a sootier methane–butene flame, the oxidation of soot by OH proceeded up to an order of magnitude faster than the oxidation of CO by OH, particularly near the flame where the soot loadings were the greatest. A subsequent correction for errors in the estimated O_2 oxidation rate of soot [34] required a revision to the estimated rates of OH oxidation of soot. The OH oxidation rates were generally revised downwards by a factor of about 2.

Taking this revision into account, the original results of Puri et al. [33] continue to indicate that the loss rate of OH by reaction with soot exceeds the loss rate with CO toward the end of their methane–butene flame, albeit in a somewhat less dramatic fashion. Figure 11 shows the calculated rate of loss of OH on soot and the rate of loss of OH by reaction with CO in the flame at 40 mm from the nozzle. The removal of OH by reaction with CO is dominant at this location. However, near the tip of the flame at 70 mm the two rates are comparable (Fig. 12). The removal of OH on soot particles is slightly smaller but of the same order of magnitude as the reaction rate with

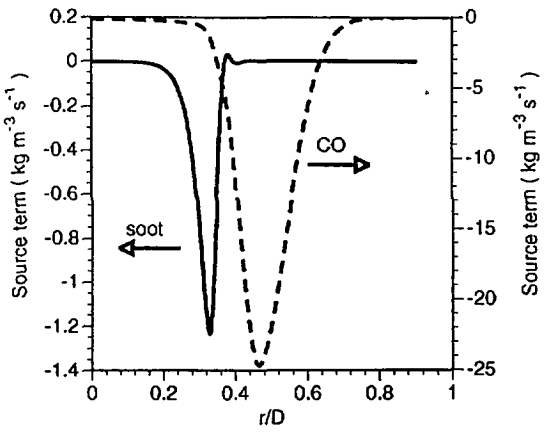

Fig. 11. Rate of loss of OH on soot (solid line); rate of loss of OH by reaction with CO (dashed line) at 40 mm from nozzle in the nonsooting flame.

CO. The results support the conclusion of Puri et al. [33] that the removal of OH on soot can be an important factor in the emission of CO from sooting flames. Unfortunately, the prediction of the rates of these reactions by simple flow field models (including turbulent flame models) is complicated by the presence of strongly superequilibrium concentrations of OH in the flames. A comparison of the calculated OH mole fractions with the equilibrium mole fractions for the same temperature revealed that the predicted mole fractions can be an order of magnitude greater than equilibrium. Substantial superequilibrium concentrations of O atoms were also predicted. This observation poses a problem for models of sooty flames that rely on equilibrium thermochemistry [9, 10].

The most difficult test for any model of soot behavior in diffusion flames is the prediction of the transition from a nonsooting to a sooting condition as the fuel flow rate is increased. The correct reproduction of the transitional behavior requires the accurate calculation of soot formation and soot burnout. This is a rigorous test of any soot model. The present code with the Fairweather et al. [11] model of soot, extended to account for OH oxidation, has been subjected to this form of testing. Experimental conditions for the sooting flame of Santoro et al. [41] were used in the calculation. Predictions and measurements of the soot volume fractions at two locations in the sooting flame of Santoro et al. [41] are shown in Figs. 13 and 14. The increased production of soot with an increased flow rate of fuel (compared to the nonsooting flame) is predicted well by the code, particularly in regard to the peak soot volume fraction. The model does not include a route to soot formation from PAH, as pointed out earlier; this contributes to the poor agreement on the axis (Fig. 14). The overall behavior of the sooting flame is best seen in the distribution of the integrated soot volume fraction along the flame (Fig. 15). The code predicts the peak soot volume fraction in the flame, but it is not able to predict correctly the

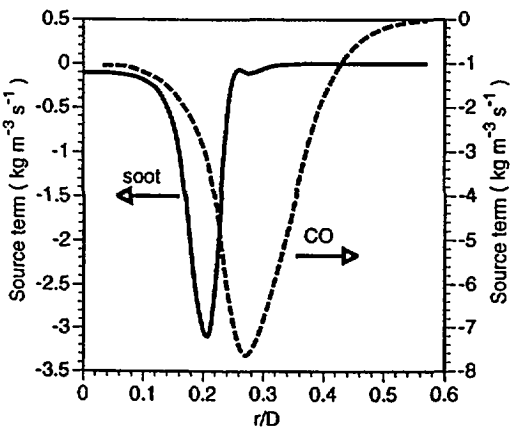

Fig. 12. Rate of loss of OH on soot (solid line); rate of loss of OH by reaction with CO (dashed line) at 70 mm from nozzle in the nonsooting flame.

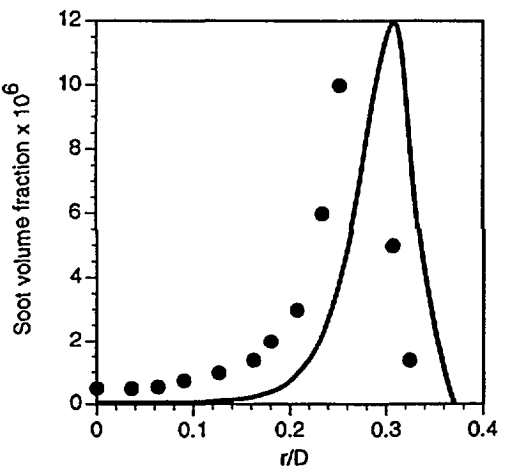

Fig. 13. Measured (Santoro et al. [41]) and predicted (solid line) soot volume fractions at 40 mm from fuel nozzle in the sooting flame.

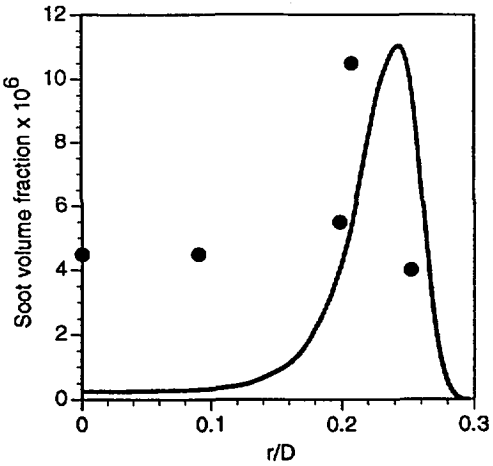

Fig. 14. Measured (Santoro et al. [41]) and predicted (solid line) soot volume fractions at 70 mm from fuel nozzle in the sooting flame.

emission of soot. The oxidation of soot proceeds too rapidly and persists too long in the cooling postflame gases. The problem lies with the oxidation rate that is calculated from the Nagle Strickland-Constable formula [30]. Evidence is available in the literature that the Nagle Strickland-Constable formula overestimates the oxidation rate of soot and char by O_2 [43, 44] at temperatures below about 1800 K; temperatures in the postflame gases are typically 1600 K or less. The accurate prediction of the transition from nonsooting to sooting flames will require an improved model for the low-temperature oxidation of soot by O_2.

One final aspect of the modeling requires mention. The use of the simple boundary layer form of the equations, together with initial conditions near the nozzle that were derived from equilibrium, eliminate the possibility of the presence of O_2 on the axis of the flame in significant amounts. However, Saito et al. [42] have found that O_2 may appear on the axis of a laminar diffusion flame, probably as a result of leakage around the burner rim. Lin et al. [45] have pointed out the large O_2 levels found by some authors may result from the coelution of argon with O_2 from GC columns.

Mass spectrometer measurements of O_2 in the nonsooting flame were obtained but are not shown here. Oxygen mass fractions between 0.001 and 0.003 were measured on the axis of the flame. O_2 may be an important oxidizer in regions that are fuel rich, although estimates of this oxidation rate based on the Nagle Strickland-Constable formula at relatively low temperatures are uncertain. Much more intensive computations with an elliptic code would be required to include the details of flow and reaction around the base of the flame. Nevertheless, some observations can be made with regard to the relative action of OH and O_2 in the oxidation of soot. The rates of oxidation of soot by each species are shown in Fig. 16.

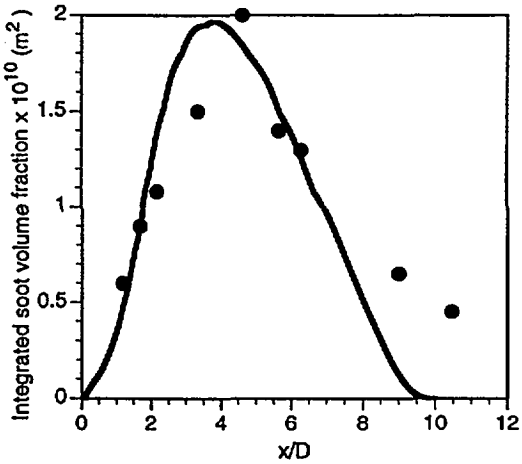

Fig. 15. Integrated soot volume fractions in the sooting flame (points are from Santoro et al. [41]).

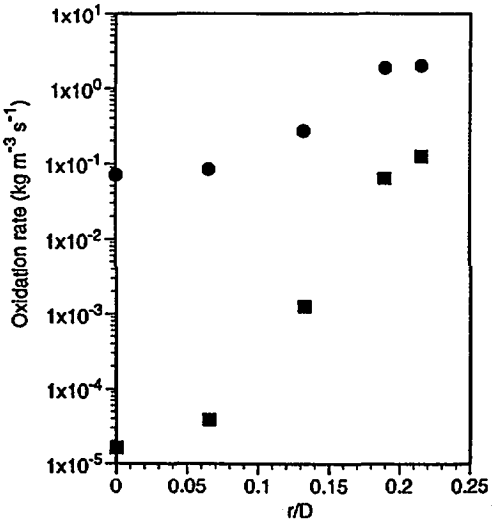

Fig. 16. Rates of soot oxidation in the nonsooting flame at 70 mm from nozzle: ■ O_2; ● OH.

The overprediction of the OH mole fractions suggests that the rates that are shown in Fig. 16 may be an upper limit to the actual OH oxidation rate of soot. Nevertheless, the rate of OH oxidation is clearly significant in relation to the O_2 rate in these regions of the flame. Puri et al. [34], in their corrected analysis of the results of Puri et al. [33], found that the maximum inferred OH oxidation rate of soot was of about 0.36 kg m^{-3} s^{-1} in a methane–butene flame. This value is lower than the maximum peak value shown in Fig. 16, possibly as a result of different flame and fuel conditions and also the overprediction of OH. They reported ratios of the rates of OH/O_2 oxidation of soot that were similar in magnitude. The numerical results at the end of the flame indicate much higher ratios. The discrepancy highlights the uncertainty that continues to surround the rates of soot oxidation, although the results confirm the importance of OH as an oxidant of soot in diffusion flames.

CONCLUSIONS

The interaction of soot and flame chemistry has been modeled with a relatively simple description of the relevant fluid and chemical processes. The inclusion of OH in the model as an oxidant of soot required the adjustment of the soot growth rates by a factor of 2 in order to achieve satisfactory agreement with measured soot volume fractions. A comparison of the numerical results with detailed experimental results indicates that the flame structure is reproduced quite well. The collision efficiency was increased with distance along the flame in a manner consistent with experimental results. The use of this ad hoc model points out the need for improved descriptions of OH oxidation of soot in diffusion flames. Furthermore, an attempt to predict the transition of a diffusion flame from a nonsooting condition to a sooting condition was only partially successful. Excessive rates of oxidation were primarily due to the overprediction of rates by the Nagle Strickland-Constable formula in the postflame region; overprediction of OH mass fractions may also have contributed to a lesser extent. A more accurate model for O_2 oxidation at low temperatures is required. The predictions confirm the importance of OH as an oxidant of soot in diffusion flames.

The inclusion of soot in the description of a diffusion flame has a significant impact on the structure of the flame. The rate of reaction of OH with soot was generally smaller than the rate of reaction with CO, but it became comparable near the tip of the flame where soot loadings were substantial. Competition for OH between soot and CO in the burnout region can be significant.

The group at Davis gratefully acknowledge the support of the National Institute of Standards and Technology through Grant 60NANBOD1055 and the National Institute of Environmental Health Sciences Superfund Basic Research Program 2 P42 ES04699. The help of Professor H. Dwyer with some aspects of the numerics is sincerely appreciated.

The research at The Pennsylvania State University was supported under grant F49620-92-J-0161 from the Air Force Office of Scientific Research (AFOSR) and grant 60NANBOD1035 from the National Institute of Standards and Technology. One of the authors (DCR) thanks the Air Force Research in Aero Propulsion Technology Program for support during his tenure.

REFERENCES

1. Mauss, F., Trilken, B., Breitbach, H., and Peters, N. In *Soot Formation in Combustion* (H. Bockhorn, Ed.), Springer Verlag, Berlin, 1994, pp. 325–349.
2. Lindstedt, P. R., In *Soot Formation in Combustion* (H. Bockhorn, Ed.), Springer-Verlag, Berlin, 1994, pp. 417–439.
3. Frenklach, M., and Wang, H., In *Soot Formation in Combustion* (H. Bockhorn, Ed.), Springer-Verlag, Berlin, 1994, pp. 162–190.
4. Frenklach, M., Wang, H., and Rabinowitz, M. J., *Progress in Energy and Combustion Science* 18:47–73 (1992).
5. Frenklach, M., and Wang, H., *Twenty-Third Symposium (International) on Combustion*, The Combustion Institute, Pittsburgh, PA, 1990, pp. 1559–1566.
6. Kaplan, C. R., Baek, S. W., Oran, E. S., and Ellzey, J. L., *Combust. Flame* 96:1–21 (1994).
7. Sivathanu, Y. R., and Gore, J. P., *Combust. Flame* 97:161–172 (1994).
8. Puri, R., Moser, M., Santoro, R. J., and Smyth, K. C., *Twenty-Fourth Symposium (International) on Combustion*, The Combustion Institute, Pittsburgh, 1992, pp. 1015–1022.

9. Villasenor, R., and Kennedy, I. M., *Twenty-Fourth Symposium (International) on Combustion*, The Combustion Institute, Pittsburgh, 1992, pp. 1023–1030.
10. Kennedy, I. M., Kollmann, and Chen, J.-Y., *Combust. Flame* 81:73–85 (1990).
11. Fairweather, M., Jones, W. P., Ledin, H. S., and Lindstedt, R. P., *Twenty-Fourth Symposium (International) on Combustion*, The Combustion Institute, Pittsburgh, PA, 1992, pp. 1067–1074.
12. Mauss, F., Schäfer, T., and Bockhorn, H., *Combust. Flame* 99:697–705 (1994).
13. Koylu, U. O., Faeth, G. M., Farias, T. L., and Carvalho, M. G., *Combust. Flame* 100:621–633 (1995).
14. Santoro, R. J., Semerjian, H. G., and Dobbins, R. A., *Combust. Flame* 51:203–218 (1983).
15. Bockhorn, H., Fetting, F., and Wenz, H. W., *Ber. Bunsen Gesell. Phys. Chem.* 87:1067–1073 (1983).
16. Fristrom, R. M., Prescott, R., and Grunfelder, C., *Combust. Flame* 1:102–113 (1957).
17. Smith, S., and Gordon, A. S., *J. Phys. Chem.* 60:759–763 (1956).
18. Mitchell, R. E., Ph.D. Thesis, MIT, 1975.
19. Crowhurst, D., and Simmons, R. F., *Combust. Flame* 59:167–176 (1985).
20. Smyth, K. C., Miller, J. H., Dorfman, R. C., Mallard, W. G., and Santoro, R. J., *Combust. Flame* 62:157–181 (1985).
21. Puri, R., Ph.D. Thesis, The Pennsylvania State University, 1992.
22. Ermolin, N. E., Korobeinichev, O., Tereshchenko, A., and Fomin, V. M., *Combust. Explosion Shock Waves* 18:36–38 (1982).
23. Bittner, J. D., Ph.D. Thesis, MIT, 1981.
24. Smooke, M. D., Xu, Y., Zurn, R. M., Lin, P., Frank, J. H., and Long, M. B., *Twenty-Fourth Symposium (International) on Combustion*, The Combustion Institute, Pittsburgh, PA, 1992, pp. 813–821.
25. Kee, R. J., Dixon-Lewis, G., Warnatz, J., Coltrin, M. E., and Miller, J. A., *A FORTRAN Computer Code Package for the Evaluation of Gas Phase Multicomponent Transport Properties*, SAND 86-8246, Sandia National Laboratories, Livermore, CA, 1992.
26. Talbot, L., Cheng, R. K., Schefer, R. W., and Willis, D. R., *J. Fluid Mech.* 101:737–758 (1980).
27. Fairweather, M., Jones, W. P., and Lindstedt, R. P., *Combust. Flame* 89:45–64 (1992).
28. Shen, C., *J. Coll. Inter. Sci.* 127:104–115 (1989).
29. de la Mora, J. F., and Rosner, D. E., *J. Fluid Mech.* 125:379–395 (1982).
30. Nagle, J., and Strickland-Constable, R. F., *Fifth Carbon Conference*, Pergamon, Oxford, 1962, pp. 154–164.
31. Neoh, K. G., Howard, J. B., and Sarofim, A. F., *Particulate Carbon Formation During Combustion*, Plenum, New York, 1981, pp. 261–282.
32. Roth, P., Brandt, O., and Gersum, S. v., *Twenty-Third Symposium (International) on Combustion*, The Combustion Institute, Pittsburgh, PA, 1990, pp. 1485–1491.
33. Puri, R., Santoro, R. J., and Smyth, K. C., *Combust. Flame* 97:125–144 (1994).
34. Puri, R., Santoro, R. J., and Smyth, K. C., *Combust. Flame* 102:226–228 (1995).
35. Williams, F. A., *Combustion Theory*, Benjamin/Cummings, Menlo Park, CA, 1985.
36. Reynolds, W. C., *STANJAN*, Department of Mechanical Engineering, Stanford University, 1986.
37. Smooke, M. D., Puri, I. K., and Seshadri, K., *Twenty-First Symposium (International) on Combustion*, The Combustion Institute, Pittsburgh, 1986, pp. 1783–1792.
38. Leung, K. M., and Lindstedt, R. P., *Combust. Flame* 102:125–160 (1995).
39. Kee, R. J., Rupley, F. M., and Miller, J. A., *CHEMKIN II: A FORTRAN Chemical Kinetics Package for the Analysis of Gas-Phase Chemical Kinetics*, SAND 89-8009, Sandia National Laboratories, Livermore, CA, 1991.
40. Smooke, M. D., and Giovangigli, V., *Impact Comp. Sci. Engr.* 4:46–79 (1992).
41. Santoro, R. J., Yeh, T. T., Horvath, J. J., and Semerjian, H. G., *Combust. Sci. Tech.* 53:89–115 (1987).
42. Saito, K., Williams, F. A., and Gordon, A. S., *ASME Transactions on Heat Transfer* 108:640–648 (1985).
43. Levendis, Y. A., Flagan, R. C., and Gavalas, G. R., *Combust. Flame* 76:221–241 (1989).
44. Chan, M.-L., Moody, K. N., Mullins, J. R., and Williams, A., *Fuel* 66:1694–1698 (1987).
45. Lin, K.-C., Sunderland, P. B., and Faeth, G. M., *Combust. Flame*. 104:369–375 (1996).

Received 30 July 1995